Materials Transactions, Vol. 61, No. 11 (2020) pp. 2101 to 2106

他誌発表論文　再録
公益社団法人日本金属学会, Materials Transactions, Vol. 61 (11) p. 2101-2106 (2020)

Hot Compression Behavior of Mg–14Li–6Al–1Ca Alloy

Ryo Tsukane[1], Hiroyasu Tamai[1], Masahiro Nogawa[2], Yoshihisa Harada[3], Kunio Matsuzaki[3] and Takashi Nagoshi[3]

[1]*Tottori Institute of Industrial Technology, Yonago 689-3522, Japan*
[2]*Kikusui Forging Ltd., Yonago 683-0851, Japan*
[3]*National Institute of Advanced Industrial Science and Technology, Tsukuba 305-8564, Japan*

The hot deformation behavior of a Mg–14Li–6Al–1Ca alloy was studied using the hot compression true stress–strain curves corresponding to the temperature range of 473–673 K at strain rates of 1×10^{-1}–1×10^{-3} s^{-1}. The true stress–strain curves indicated dynamic softening under the test conditions. The peak stress during deformation could be correlated with the temperature and strain rate using a hyperbolic-sine equation. The activation energy of the Mg–14Li–6Al–1Ca alloy was determined to be 193 kJ mol^{-1}. The Zener-Hollomon parameter (Z) for the Mg–14Li–6Al–1Ca alloy was determined. The tendency for dynamic recrystallization increases at low strain rates and high temperatures, corresponding to low Z values. The hot deformation behavior of the Mg–14Li–6Al–1Ca alloy was modelled by a suitable constitutive equation. Furthermore, the size of the equiaxed grains in the hot-deformed and quenched specimens was estimated from the Z value.
[doi:10.2320/matertrans.MT-M2020157]

(Received May 19, 2020; Accepted August 3, 2020; Published October 25, 2020)

Keywords: *magnesium–lithium alloy, hot deformation, Zener-Hollomon parameter, activation energy, dynamic recrystallization*

1. Introduction

Magnesium alloys are known for their low density and high strength to weight ratio, resulting in a high demand from industries such as transportation and electric appliances. Magnesium–lithium (Mg–Li) alloys have a lower density than other magnesium alloys. The addition of lithium ($>\sim$11 mass% (30 at%)) to magnesium causes the crystal structure to transform from hcp α phase to single bcc β phase. The bcc β phase is soft and ductile, leading to increased deformability. The mechanical properties and the plastic deformation of Mg–Li alloys at room temperature have long been investigated.[1–13] However, high temperatures are necessary for any deformation involving complex and large shapes, even if the original Mg–Li alloys are soft and ductile. To date, there is very little information about the hot compression deformation behavior of Mg–Li alloys. If dynamic recrystallization occurs during high-temperature deformation, the flow stress will decrease and thus, plastic deformation becomes easier. Further, the achievement of an equiaxed crystal grain via recrystallization can improve various mechanical properties of the alloy such as its strength and ductility.

To study the hot compression behavior, it is important to understand the flow stress and microstructure evolution. The Zener-Hollomon parameter is often used to understand the flow stress of high-temperature compression deformation,[14,15] since it establishes a correlation between temperature, strain rate, and flow stress. Several studies have reported that it is possible to optimize the microstructural evolution.[16–19] The processing conditions by which the grains become equiaxed after deformation were estimated using the Zener-Hollomon parameter.

This study is, therefore, devoted to the investigation of the hot deformation behavior of a Mg–Li–Al–Ca four-element-based alloy (Al and Ca were added to improve the alloy's mechanical properties). Analysis was performed by tuning the Zener-Hollomon parameter to control the grain structure obtained by deformation and recrystallization and to improve the mechanical properties of the alloy. The relationship between the Zener-Hollomon parameter and the microstructural evolution in the hot-deformed specimens has also been determined.

2. Experimental Procedure

2.1 Process and materials

2.1.1 Materials

The as-received Mg–14Li–6Al–1Ca alloy was an extruded round rod with a diameter of 15 mm, obtained from Santoku Co. Ltd., Japan. The chemical composition of the alloy is given in Table 1. Cylindrical specimens of 10 mm diameter and 15 mm height were machined from the as-received rod. Phase information were obtained by a X ray diffraction (XRD), using a Ultima IV (Rigaku, Japan).

2.1.2 Process

Hot compression tests of the specimens were performed on an MTS-810 system (MTS, US) by maintaining the furnace within a temperature range of 473–673 K at a strain rate in the range of 1×10^{-1}–1×10^{-3} s^{-1}. After soaking for 5 min in the above temperature range, hot compression was performed up to a true strain of 0.7. Then, the specimens were immediately quenched in water to preserve the hot deformation microstructure. The hot-deformed specimens were cut in a direction parallel to the compression direction and were examined by optical microscopy after etching in 2% nitric acid in ethanol. The average grain size of the samples was measured by the linear intercept method using the following equation:[20]

$$D = 1.74L/n_L, \tag{1}$$

where L is the total length of the lines used and n_L is the number of grains crossed through by the lines.

Table 1 Chemical compositions of Mg–Li–Al–Ca alloy (in mass%).

Mg	Li	Al	Ca	Zn	Si	Fe	Cu	Ni	Mn
Bal.	13.98	5.60	0.98	0.002	0.017	<0.001	<0.001	<0.001	0.120

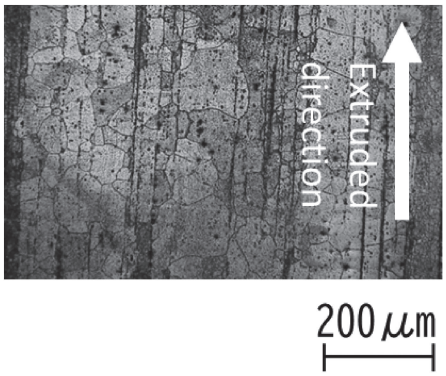

Fig. 1 Initial microstructure of the Mg–Li–Al–Ca alloy.

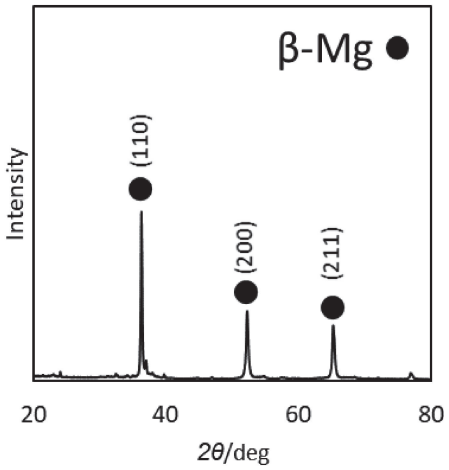

Fig. 2 X-ray diffraction pattern of Mg–14Li–6Al–1Ca alloy.

3. Results and Discussion

3.1 Microstructure and composition of the as-received alloy

The initial microstructure of the as-received alloy is shown in Fig. 1. The microstructure exhibits a mixture of coarse and fine grains, with the average grain size of the coarse grains being approximately 50–80 μm. Figure 2 displays the X-ray diffraction pattern of the as-received Mg–14Li–6Al–1Ca alloy, where the basic microstructural constituent of the alloy is seen to be the β phase (Li).

3.2 True stress–strain curves

The true stress–strain curves, obtained by the hot compression testing, are presented in Fig. 3. Since the flow stress decreases with the increase in temperature and decrease in strain rate, it is evident that the flow stress is affected by the strain rate and temperature. At a given strain rate, by increasing the strain, the flow stress first increases up to a maximum and then decreases to a steady state. It is suggested that dynamic softening[21] occurred in a temperature range of 473–673 K. Further, it may also be considered that some stress oscillations occur under particular processing conditions.

3.3 Microstructures of the deformed Mg–14Li–6Al–1Ca alloy

The typical microstructures of the Mg–14Li–6Al–1Ca alloy deformed under the true strain value of 0.7 at a strain rate of $1 \times 10^{-3}\,s^{-1}$ in the temperature range of 473–673 K are shown in Fig. 4. At the lowest temperature of 473 K and a strain rate of $1 \times 10^{-3}\,s^{-1}$, the original grains were elongated perpendicular to the compression direction and there was no apparent recrystallization (Fig. 4(a)). Figures 4(b)–(d) illustrate the microstructures of the specimens hot deformed at 573–673 K and $1 \times 10^{-3}\,s^{-1}$ strain rate. In this case, compared with the grain size of the primary microstructure in Fig. 1, the average grain size changed, and the grains were equiaxed. At the temperature of 573 K (Fig. 4(b)), the grain sizes were almost the same as those observed in 623 K (Fig. 4(c)). Coarsening occurred at the temperature of 673 K. Grain refinement occurred during the hot deformation process owing to dynamic recrystallization, thereby implying that grain refinement may also occur in Mg–14Li–6Al–1Ca alloys depending on the processing conditions.

3.4 Constitutive equations for the flow stress of the Mg–14Li–6Al–1Ca alloy

Constitutive equations were used to calculate the activation energy and hot deformation constants of the Mg–14Li–6Al–1Ca alloy. The base equation is shown in eq. (2). In this equation, the Zener-Hollomon parameter (Z) is the temperature-compensated strain rate.

$$Z = \dot{\varepsilon} \exp(Q/RT) = F(\sigma) \tag{2}$$

Here, $\dot{\varepsilon}$ is the strain rate, Q is the activation energy of deformation, R is gas constant ($8.314\,J \cdot mol^{-1} \cdot K^{-1}$), and T is the temperature.

As seen in eq. (2), the Z parameter is also a function of stress. The relationship between Z and stress is dependent on the stress regime. The power law description of stress (eq. (3)) is preferred for relatively low stress values. Conversely, the exponential law (eq. (4)) is only suitable for high stresses. However, the hyperbolic sine law (eq. (5)) can be used for a wide range of temperatures and strain rates.[22]

$$F(\sigma) = A' {\sigma_p}^{n_1} \tag{3}$$

$$F(\sigma) = A'' e^{\beta \sigma_p} \tag{4}$$

$$F(\sigma) = A[\sinh(\alpha \sigma_p)]^n \tag{5}$$

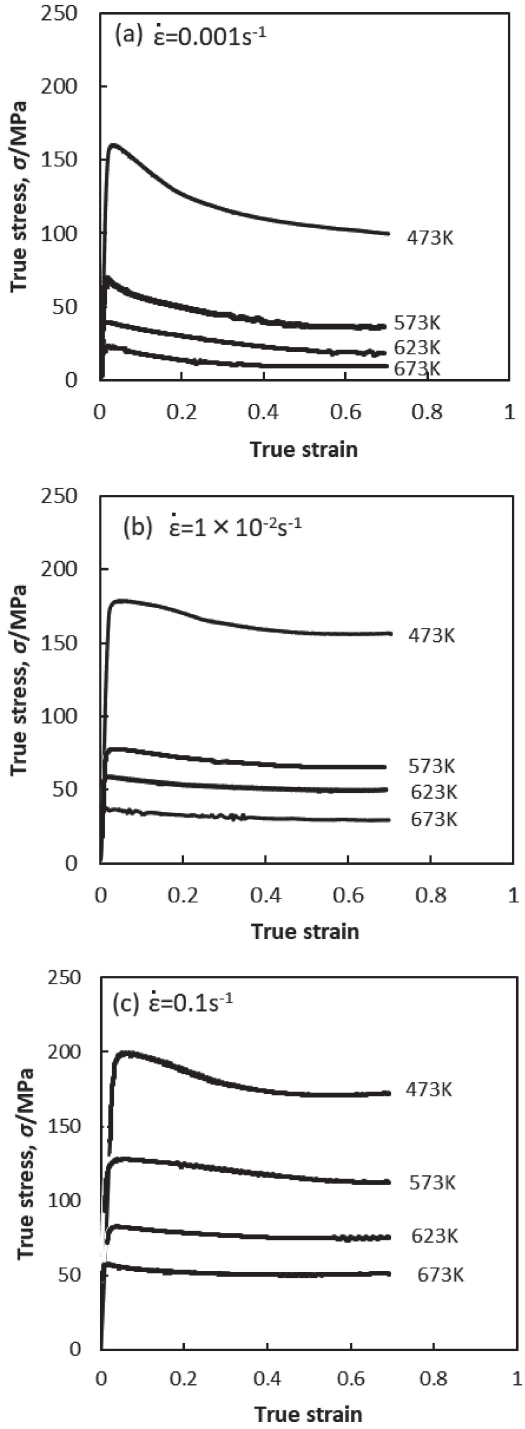

Fig. 3 Compression true stress–strain curves for the Mg–14Li–6Al–1Ca alloy under various deformation conditions.— (a) $\dot{\varepsilon} = 0.001\,s^{-1}$, (b) $\dot{\varepsilon} = 0.01\,s^{-1}$, and (c) $\dot{\varepsilon} = 0.1\,s^{-1}$.

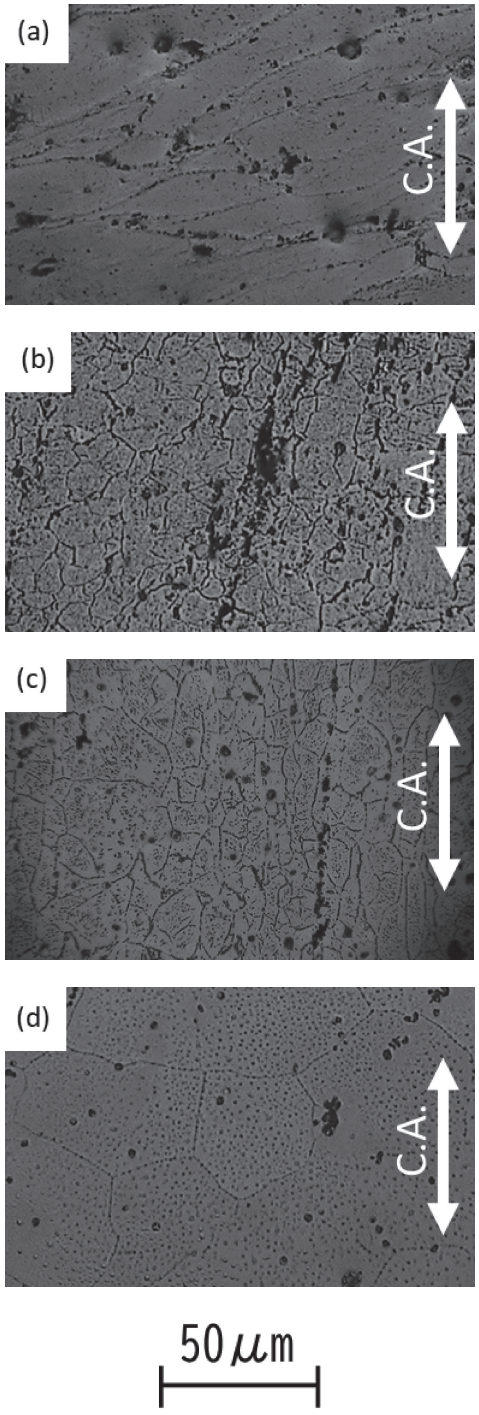

Fig. 4 Microstructures of alloy subjected to different deformation conditions.— (a) 473 K, $1 \times 10^{-3}\,s^{-1}$, (b) 573 K, $1 \times 10^{-3}\,s^{-1}$, (c) 623 K, $1 \times 10^{-3}\,s^{-1}$, (d) 673 K, $1 \times 10^{-3}\,s^{-1}$, where C.A. means the compression axis.

Here A, A', A'', α (where $\alpha \approx \beta/n_1$), β, n, and n_1 are apparent material constants, and σ_p is the peak stress. For eqs. (3)–(5), the steady stress is generally used, however, the peak stress may also by used.[15,16,21] By substitution of F(σ) from eqs. (3)–(5) into eq. (2) and by taking the natural logarithm from each side of the resulting equations, the following expressions were derived for the peak stress:

$$\ln \dot{\varepsilon} + Q/RT = \ln(A') + n_1 \ln(\sigma_p), \tag{6}$$

$$\ln \dot{\varepsilon} + Q/RT = \ln(A'') + \beta\sigma_p, \tag{7}$$

$$\ln \dot{\varepsilon} + Q/RT = \ln(A) + n \ln[\sinh(\alpha\sigma_p)]. \tag{8}$$

At a constant deformation temperature, and assuming the activation energy as a constant parameter, partial differentiation of eqs. (6)–(8) yielded the following equations, respectively:

$$n_1 = \left[\frac{\partial \ln \dot{\varepsilon}}{\partial \ln \sigma_p}\right]_T \tag{9}$$

$$\beta = \left[\frac{\partial \ln \dot{\varepsilon}}{\partial \sigma_p}\right]_T \tag{10}$$

$$n = \left[\frac{\partial \ln \dot{\varepsilon}}{\partial \ln[\sinh(\alpha\sigma_p)]}\right]_T \tag{11}$$

The slope of the plot of $\ln \dot{\varepsilon}$ versus $\ln \sigma_p$, and the slope of the plot of $\ln \dot{\varepsilon}$ versus σ_p were used to obtain the values of n' and β, respectively. These plots are shown in Fig. 5(a) and (b). The linear regression of these data resulted in the average values of 5.9 and 0.10 for n_1 and β, respectively, yielding a value of $\alpha = \beta/n_1 = 0.017$. According to eq. (11), the slope of the plot of $\ln \dot{\varepsilon}$ versus $\ln \sinh(\alpha\sigma_p)$ was used to obtaining the value of n (Fig. 5(c)). The average value of n was determined to be 4.96.

At a constant strain rate, the partial differentiation of eq. (8) yields the following equation:

$$Q = Rn\left[\frac{\partial \ln[\sinh(\alpha\sigma_p)]}{\partial(1/T)}\right]_{\dot{\varepsilon}} = Rnp \tag{12}$$

Thus, p is the value of the slope of the plot of $\ln \sinh[(\alpha\sigma_p)]$ versus the reciprocal of the absolute temperature. This plot is shown in Fig. 5(d). The linear regression of this data resulted in an average value of 4.68 for p and a value of 193 kJ mol^{-1} for the activation energy from eq. (12).

Taking the natural logarithm of eq. (5), the following expression was derived:

$$\ln Z = \ln A + n \ln[\sinh(\alpha\sigma_p)] \tag{13}$$

The resulting plot is shown in Fig. 6. The linear regression of this data resulted in values of 5.11 and 31.8 for n and $\ln A$, respectively. Hence, the relation between Z and σ_p was obtained as follows:

$$Z = \dot{\varepsilon} \exp(-193000/RT) = e^{31.8}[\sinh(0.017\sigma_p)]^{5.11} \tag{14}$$

From this equation, the flow stress was estimated from the temperatures and strain rates. Figure 7 shows the correlation between calculated and measured stress values, where the flow stress was accurately estimated.

3.5 Relationship between the Zener-Hollomon parameter and the microstructures of the deformed Mg–14Li–6Al–1Ca alloy

The softening processes of recovery and recrystallization occur during deformation at high temperatures in many alloys, and the resulting microstructure of the deformed alloys is dependent on the processing conditions. The true stress–strain curves of the Mg–14Li–6Al–1Ca alloy (Fig. 3) show a steady-state flow stress, indicating that softening occurred as a result of dynamic restoration which cancelled work hardening. Dynamic recovery may occur at higher Z values because at these values the alloy is composed of the deformed initial grains (Fig. 4(a)). On the other hand, dynamic recrystallization may occur at lower Z values because the alloy is composed of equiaxed grains surrounded by clear grain boundaries instead of initial grains (Fig. 4(b)–(d)). The possibility of expressing dynamic recrystallization using Z was examined. Figure 8 depicts the relationship between Z and the strain rate, temperature, and deformation structure. As outlined by the solid lines in Fig. 8, the

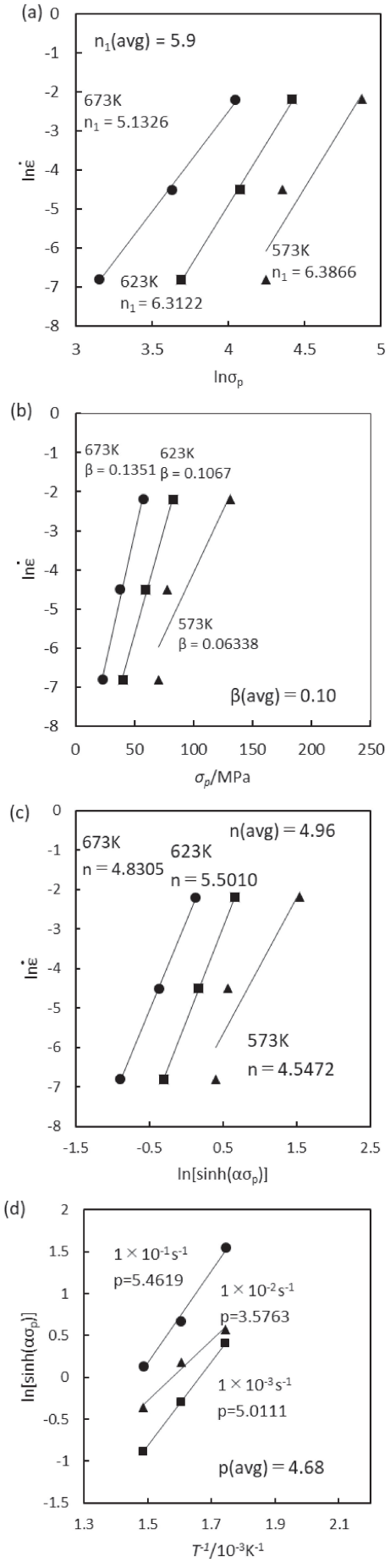

Fig. 5 Plots depicting (a) $\ln \dot{\varepsilon}$ vs. $\ln \sigma_p$, (b) $\ln \dot{\varepsilon}$ vs. σ_p, (c) $\ln \dot{\varepsilon}$ vs. $\ln[\sinh(\alpha\sigma_p)]$, and (d) $\ln[\sinh(\alpha\sigma_p)]$ vs. $1/T$.

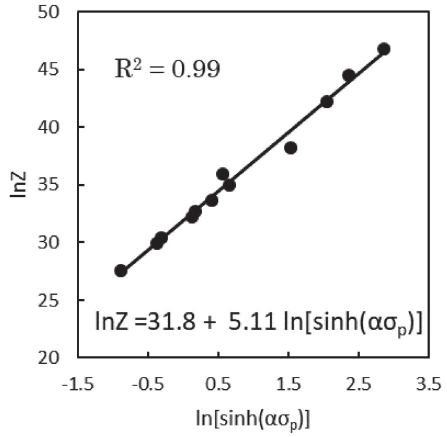

Fig. 6 Relationship between $\ln Z$ and $\ln[\sinh(\alpha\sigma_p)]$.

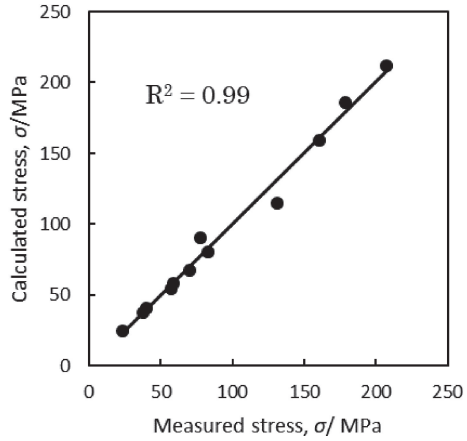

Fig. 7 Comparison between calculated and measured stress.

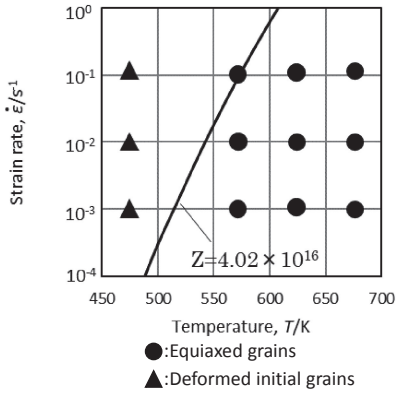

Fig. 8 Relationship between deformation structure and the Zener-Hollomon parameter for the following conditions.

boundary Zc between the deformation condition regions where the grains are elongated perpendicular to the compression direction and the deformation condition regions where the grains become equiaxed, exists in the range of $4.02 \times 10^{16}\,s^{-1} < Zc$. Under the deformation condition of $Z > Zc$, the elongated initial grains were retained, whereas under the deformation condition of $Z < Zc$, dynamic recrystallization occurred, changing the shape of grain to equiaxed. Thus, the microstructure of the deformed Mg–14Li–6Al–1Ca alloy could be determined using Z.

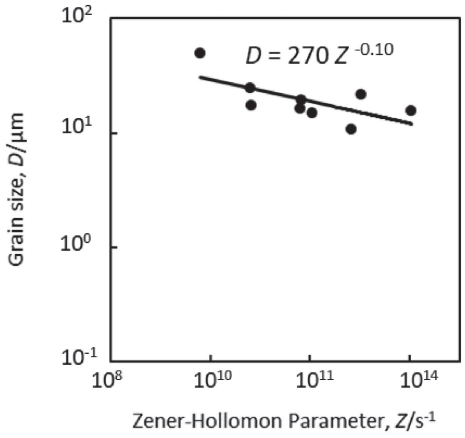

Fig. 9 Relationship between the Zener-Hollomon parameter and the equiaxed grain sizes in hot-deformed and quenched specimens.

The relationship between Z and the equiaxed grain sizes in hot-deformed and quenched specimens is shown in Fig. 9. From these results, the following relationship between grain size and Z was estimated:

$$D = AZ^{-n} \tag{15}$$

where D is the grain size, A is a constant, and n is the power law exponent.

This equation has been used to predict the dynamic recrystallization grain size in other Mg alloys. In the present work, the values of A and n were determined to be 270 and 0.10, respectively. Values of A and n were reported in the range of 498–760 and 0.09–0.16, respectively, for alternative Mg alloys.[23–25] This indicates that grain refinement for a Mg–14Li–6Al–1Ca alloy can be performed at the same deformation conditions necessary for popular Mg alloys such as AZ31 or AZ91.

4. Conclusions

This work has focused on the influence of the deformation conditions on the hot deformation behavior of a Mg–Li–Al–Ca four-element-based alloy. The key conclusions of the study are as follows:

(1) The true stress–strain curves of the Mg–14Li–6Al–1Ca alloy, over the wide range of temperatures and strain rates investigated in this study, exhibited a single peak stress, followed by a gradual fall towards a steady-state stress.

(2) The activation energy of the Mg–14Li–6Al–1Ca alloy was determined to be $193\,kJ\,mol^{-1}$.

(3) The peak stress of the Mg–14Li–6Al–1Ca alloy in a temperature range of 573–673 K and a strain rate range of $1 \times 10^{-1}\,s^{-1}$–$10^{-3}\,s^{-1}$ could be accurately estimated from the temperatures and strain rates. The following constitutive equation was used to express the hot working characteristics of the investigated alloy:

$$Z = \dot{\varepsilon}\exp(-193000/RT) = e^{31.8}[\sinh(0.017\sigma_p)]^{5.11} \tag{16}$$

(4) Dynamic recrystallization occurred under the condition of $Z < 4.02 \times 10^{16}\,s^{-1}$.

(5) The equiaxed crystal grain size could be estimated from the following equation:

$$D = 270Z^{-0.10}. \quad (17)$$

Acknowledgments

This research was partially supported by project "Chiiki sangyo kasseika jinzai ikusei shien jigyo" of the National Institute of Advanced Industrial Science and Technology (AIST).

REFERENCES

1) Y. Kojima, M. Inoue and O. Tanno: J. Japan Inst. Metals. **54** (1990) 354–355.
2) W. Fujitani, K. Higashi, N. Furushiro and Y. Umakoshi: J. JILM **45** (1995) 333–338.
3) H. Dong, F. Pan, B. Jiang, R. Li and X. Huang: Mater. Des. **65** (2015) 42–49.
4) K. Matsuzawa, T. Koshihara, S. Ochiai and Y. Kojima: J. JILM **39** (1989) 45–51.
5) K. Matsuzawa, T. Koshihara, S. Ochiai and Y. Kojima: J. JILM **40** (1990) 659–665.
6) S.S. Nene, B.P. Kashyap, N. Prabhu and Y. Estrin: J. Alloy. Compd. **615** (2014) 501–506.
7) L.R. Cheng, Z.Y. Cao, Y.B. Liu, L. Zhang, T.Q. Li and G.H. Su: Mater. Trans. **51** (2010) 2325–2328.
8) R. Ninomiya and K. Miyake: J. JILM **51** (2001) 509–513.
9) M. Kasatani, K. Tamai, A. Nishimura, T. Konno, S. Katsura and H. Yamamoto: Sokeizai **55** (2014) 39–43.
10) O. Sivakesavam and Y.V.R.K. Prasad: Mater. Sci. Eng. A **323** (2002) 270–277.
11) S. Hori and W. Fujitani: J. JILM **40** (1990) 285–289.
12) Y. Yoshida, H. Yamada, S. Kamado and Y. Kojima: J. JILM **51** (2001) 551–555.
13) M. Furui, C. Xu, T. Aida, M. Inoue, H. Anada and T.G. Langdon: J. Japan Inst. Metals. **70** (2006) 729–734.
14) C. Zener and J.H. Hollomon: J. Appl. Phys. **15** (1944) 22–32.
15) H. Mirzadeh, J.M. Cabrera, J.M. Prado and A. Najafizadeh: Mater. Sci. Eng. A **528** (2011) 3876–3882.
16) M. Jafari and A. Najafizadeh: Mater. Sci. Eng. A **501** (2009) 16–25.
17) M. Nishimoto, W. Takahashi and Y. Shida: Tetsu-to-Hagané **78** (1992) 1398–1405.
18) F. An, Y. Sha, F. Zhang and L. Zuo: Acta Metall. Sin. (Engl. Lett.) **24** (2011) 1–8.
19) J. Zhang, H. Di, H. Wang, K. Mao, T. Ma and Y. Cao: J. Mater. Sci. **47** (2012) 4000–4011.
20) A.W. Thompson: Metallography **5** (1972) 366–369.
21) F.J. Humphreys and M. Hatherly: *Recrystallization and Related Annealing Phenomena*, second edition, (Elsevier, UK, 2004).
22) C.M. Sellars and W.J.McG. Tegart: Mem. Sci. Rev. Met. **63** (1966) 731–746.
23) A.G. Beer: PhD Thesis, Deakin University, Deakin, Austria, (2004).
24) S.M. Fatemi-Varzaneh, A. Zarei-Hanzaki and H. Beladi: Mater. Sci. Eng. A **456** (2007) 52–57.
25) G.R. Ebrahimi, A.R. Maldar, R. Ebrahimi and A. Davoodi: J. Alloy. Compd. **509** (2011) 2703–2708.